Journal of Aerosol Science 165 (2022) 106042

Contents lists available at ScienceDirect

Journal of Aerosol Science

journal homepage: www.elsevier.com/locate/jaerosci

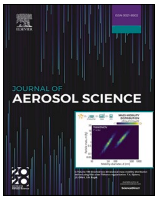

A quantitative criterion to predict atomic disordering during high velocity nanoparticle impact

T.V. Chitrakar [a], Michael F. Becker [a,b,*], Desiderio Kovar [a,c]

[a] Materials Science and Engineering Program, The University of Texas at Austin, Austin, TX, 78712, USA
[b] Department of Electrical and Computer Engineering, The University of Texas at Austin, Austin, TX, 78712, USA
[c] Department of Mechanical Engineering, The University of Texas at Austin, Austin, TX, 78712, USA

ARTICLE INFO

Keywords:
Aerosol nanoparticle deposition
Solid-state disordering
Amorphization
Silver nanoparticles
Molecular dynamics

ABSTRACT

Particle deformation at impact is a critical parameter for film formation using aerosol deposition processes for sub-micron particles. Here we study the necessary criteria to initiate atomic disorder during particle impact that can lead to deformation via viscous flow. Molecular dynamics simulations were conducted to test the hypothesis that disordering of individual silver atoms occurs under non-uniform, high strain rate loading when a critical potential energy/atom (PE/atom) of −2.72 eV is exceeded. To test this hypothesis, simulations of Ag nanoparticles impacting a flat Ag substrate were conducted for impact velocities of 100, 300, and 600 m/s, and the PE/atom and the atomic configurations for atoms positioned at different locations within the nanoparticles were tracked over time. The results showed that atoms that disorder or do not disorder could be correctly predicted by the PE/atom. A statistically varying time differential was observed between the time amorphization was predicted and when it occurred. For the small fraction of the atoms that were borderline cases, the PE/atom and two measures of atomic disorder did not agree. The physical causes for the time differentials between predicted and observed disordering and the accuracy of prediction of disordering are discussed.

1. Introduction

Micro-cold spray (MCS, AKA aerosol deposition method and vacuum kinetic spraying) is an aerosol process that produces thick films by impacting solid, sub-micron particles onto substrates at high velocity. There have many examples of experimental studies where high density, adherent ceramic and metal films have been demonstrated using micro-cold spray (Akedo et al., 2003; Hanft et al., 2015; Park et al., 2015), but there have been comparatively few studies aimed at understanding the mechanisms for particle deformation and sticking that are responsible for film growth. We recently have shown that dislocation-driven plasticity is responsible for particle deformation in Ag particles impacting at relatively low velocities (Chitrakar et al., 2017). At faster impact velocities, the strain rates are sufficiently high that regions of both metal and ceramic particles disorder and then flow viscously (Chitrakar et al., 2019; Ogawa, 2005, 2006). These heterogenous regions of the particles appear to disorder spontaneously after experiencing large strains and high strain rates over a time scale of several picoseconds. The strains result in atomic-scale bond length changes, rotations, or bending that increase the potential energy (PE) relative to the undistorted lattice. We have previously described a physical basis for disordering from the results of MD simulations (Becker & Kovar, 2020). The factors that influence disordering are the local temperature, strain

---

* Corresponding author. Materials Science and Engineering Program, The University of Texas at Austin, Austin, TX, 78712, USA.
E-mail address: becker@uts.cc.utexas.edu (M.F. Becker).

https://doi.org/10.1016/j.jaerosci.2022.106042
Received 15 February 2022; Received in revised form 21 June 2022; Accepted 22 June 2022

magnitude, strain state, and strain rate. Since PE accounts for all of these factors and can be measured at the local atom scale, it provides a quantitative tool for assessing local energy during particle impact. We further noted that short excursions above the critical potential energy due to thermal fluctuations do not necessarily result in disordering. Disordering requires collective motions of atoms and thus, in some cases, several phonons must pass through a crystal before it is statistically likely that a disordering reaction will occur. These observations lead us to hypothesize that disordering occurs when a critical threshold PE/atom is exceeded for a sufficient time that it renders the crystal unstable.

Disordering during high strain rate deformation has also been observed by Wang et al. using MD simulations of shock-induced fracture of metallic nanowires (Wang et al., 2011). Based on their simulation results, they suggested that a correlation exists between the maximum *average* potential energy per atom and disordering. However, the deformation behavior in their samples was non-uniform due to necking and shock wave propagation, and this complicated the interpretation of how spatial variations in the average PE/atom affects disordering. In two subsequent papers, we have explored the relationships between PE/atom and disordering under *uniform* applied loading and proposed a criterion to predict disordering (Becker & Kovar, 2020, 2021). This criterion states that disordering occurs when a critical PE/atom is reached. For Ag, we demonstrated that the critical PE/atom to initiate disordering under uniform uniaxial or biaxial loading is −2.7 eV. A subsequent analysis of this data suggests that an additional significant digit for the critical PE/atom is justified, and we therefore revise our estimate of the critical PE/atom to −2.72 eV. In these previous simulations, we showed that the minimum critical value of PE/atom for disordering is the same as the PE/atom at the equilibrium melting point of Ag. Further simulations were conducted for gold, and it was shown that the minimum critical PE/atom for disordering is also equal to the PE/atom at the melting point of Au. This suggests that the critical PE/atom for disordering can be readily determined with minimal computational expense for other materials from the PE/atom at melting.

There have been few experimental studies of solid-state disordering (amorphization) caused by high strain rate deformation. This is because it is challenging to: 1) impose the very high strain rates needed to observe amorphization in engineering materials, 2) monitor the crystalline state of the lattice over the time scales that amorphization transformations occur, and 3) since *ex situ* experiments cannot be used because metals that deform readily and disorder at high strain rates, devitrify quickly. Molecular dynamics (MD) simulations can overcome these challenges because amorphization can be modeled and visualized directly at the temporal and spatial scales appropriate for the physical phenomena. For example, using MD simulations, Ikeda et al. showed that Ni amorphizes in 6–12 ps at strains of 40–70% and a strain rate of 5×10^{11} s^{-1}. (Ikeda et al., 1999).

Even under uniform uniaxial or biaxial loading, the PE/atom can locally become nonuniform, and this suggests that the critical PE/atom criterion is a leading indicator for the onset of disordering may also be applicable for cases of inhomogenous loading with nonuniform strain rates and strain states where disordering is highly localized. In this paper, we test the hypothesis that a critical PE/atom of −2.72 eV can predict high strain rate disordering, even when the strain state, strain rate, and strain magnitude are all highly non-uniform. To test this hypothesis, we present the results from MD simulations of Ag particles impacting onto flat Ag substrates at high velocities. This simulation geometry produces severe gradients in strain magnitude, strain rate, and strain state within the impacting particle. By varying the impact velocity and studying the atomic configurations at different locations within the impacting particles, a range of strains, strain states and strain rates are produced that result in locally large variations in PE/atom. This large range of PE/atom allows us to test the critical PE/atom criterion for predicting local disordering at the atomic scale under the highly nonuniform conditions experienced during particle deposition. Local atom variables (such as the bond-orientational order parameter Q6, PE/atom, PTM classification of structure, strain rate, strain state, etc.) are the basis of our analysis. Although, the substrate and NP crystal orientations play a role in *how* the local variables reach their critical values, the determination of local disordering is based solely on *whether* the local variables reach their critical values. Sufficiently varied strain states and rates are studied using by the reported simulations to demonstrate the feasibility of the PE/atom criterion. This analysis to test the hypothesis that PE/atom is a leading indicator for the onset of disordering does not consider the possibility that disordered atoms may revert to the crystalline state (devitrify). Local atom variables such as PE/atom and atomic structure measures at the time of disordering are the basis of our analysis. The particle and substrate microstructure will continue to evolve after the atoms first begin to disorder. However, devitrification does not significantly affect the final shape of the particle because the particle has stopped deforming before there is widespread devitrification. The time scale for appreciable devitrification is generally much longer (at least 10s of ps) compared to the time scale for disordering and resulting particle deformation during impact (<7 ps). Thus, the final shape and crystalline state of the particle do not play a role in whether or when atoms initially disorder.

2. Methods & simulation conditions

MD simulations of the impact of an initially face-centered cubic (FCC), spherical silver nanoparticle (NP) onto a stationary, planar silver substrate were conducted using LAMMPS (Plimpton, 1995). The simulations were implemented at the Texas Advanced Computing Center at the University of Texas at Austin. The embedded-atom-method (EAM) potential for Ag from the NIST Interatomic Potentials Repository Project was used (Williams et al., 2006). The developers of the Ag.eam.alloy potential for Ag have shown that the potential accurately reproduces the lattice parameter, cohesive energy, elastic constants, phonon frequencies, thermal expansion, lattice-defect energies, and the energies of alternate structures of Ag. (Williams et al., 2006).

The total simulation volume was 60 × 60 × 80 lattice constants (lattice constant = 0.409 nm for Ag), with the larger dimension in the z direction that corresponded to the NP impact direction. The substrate was contained within the bottom 60 × 60 × 40 lattice units (583,200 atoms). The boundary conditions in all three dimensions were periodic for the simulation volume.

Spherical particles with diameters of 4.5 nm (≈2750 atoms, example shown in Fig. 1) were impacted onto the substrate at a range of velocities. TEM observations from both our published experimental results (Huang et al., 2007) with silver NPs and by others (Kashu

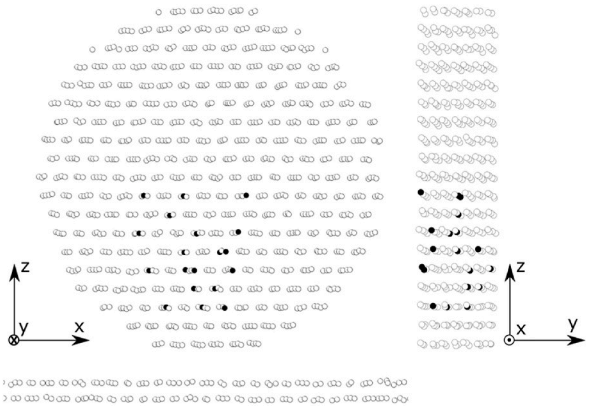

Fig. 1. A centered slice 1.1 nm thick of a 4.5 nm particle just before impact. The plane of the slice was initially {110} viewed with the <111> direction vertical (z axis). The slice was rotated by 8° about the z-axis to allow atoms that were initially shadowed along the y-axis to be visible. Locations of atoms that were tracked are indicated in solid black. The identification number of each tracked atom is shown in Table 1.

et al., 1984) confirm that the Ag NPs in this size range are spherical. The spherical shape was found to be metastable at 300 K for the typical duration of the simulations (~100 s ps). This particle size was selected because it is sufficiently large so that surface effects are not dominant but is small enough to allow particle deformation mechanisms to be studied (Chitrakar et al., 2017). For these simulations, the particle orientation was fixed such that the impact axis is oriented along [111] in the NP and the substrate surface normal is aligned along [001]. We only considered particles that were free of stacking imperfections and, consistent with experimental observations of similarly sized Ag particles, we have assumed the particles to be free of surface oxides (Huang et al., 2007).

The impacting NP was initially placed such that the bottom of the NP was 14.5 lattice units (~6 nm) above the substrate. The Ag atoms in the substrate and the impacting NP were allowed to thermalize at 300 K for 80 ps before the NP was set in motion. A constant velocity was imparted to all atoms in the impacting NP. The time integration for the equilibration of the system to 300 K and for the subsequent impact were performed with a time step of 0.001 ps (1 fs) using Nose-Hoover style, non-Hamiltonian equations of motion on the isothermal-isobaric (called npt) ensemble with a 1 ps thermal time constant for equilibration and 100 ps time constant during the impact experiment (Shinoda et al., 2004). The angular momentum of the impacting NP was set to zero at every timestep during thermalization to control particle orientation during thermalization, and the linear and angular momentum in the particle relative to the motion of the center of mass was set to zero every timestep prior to impact to preserve pre-impact orientation and to specify the impact location. After equilibration, the NP was set in motion with a -z velocity of 100, 300, or 600 m/s (≈0.006, 0.05, and 0.2 eV/atom). These velocities were selected because they are representative of impact velocities employed for particles during micro-cold spray (MCS) (McCallister et al., 2021) and laser ablation of a microparticle aerosols (LAMA) (Huang et al., 2007) film deposition processes. For our simulations, we observed that the range of impact velocities is not high enough to produce shock waves, and the back-reflected acoustic waves are negligible.

Nineteen of the atoms within the NP were selected for detailed study and the positions, velocities, and PE/atom for each chosen atom were computed at every time step and captured every 50 fs (0.05 ps) for off-line analysis. The 19 atoms were selected randomly (both in lateral and depth position) in the lower half of the slice shown in Fig. 1 with 1–4 atoms chosen in each row. Surface atoms (with differing PE/atom) were excluded, but no other variables played a role in the selection process. The region where the atoms were selected was chosen because: 1) it contains atoms that experience a wide range of strains, strain states, strain rates, and temperatures for a given impact velocity, and 2) for different impact velocities, some of the atoms disorder and some do not. These two considerations allow an assessment of the proposed disordering criterion based on PE/atom.

LAMMPS was also instructed to calculate the bond-orientational order parameter Q6 for each atom (Mickel et al., 2013; Steinhardt et al., 1983). They show how Q6 is determined by calculating an $l = 6$ bond-orientational order parameter for each atom. It is based on the sum of spherical harmonics of the bond angles for the selected atom to its neighbors (normally 12 neighbors within the selected cutoff radius). Q6 was found to be the most sensitive of the various Q parameters for discriminating between FCC, HCP, and disordered atomic configurations and because it provides a continuous, quantitative assessment of the atomic configurations that can be correlated to specific crystal structures or disordering. The theoretical values in a defect-free crystal at 0 K are Q6 = 0.575 for the FCC configuration and Q6 = 0.484 for the HCP configuration (Mickel et al., 2013). Thermal fluctuations at finite temperature affect these values, however, as evidenced by the fact that the majority of the Q6 values for FCC atoms ranged from 0.55 to 0.575, with a few extending down to 0.50. To determine the values of Q6 where transformations occur at finite temperatures, the Q6 parameter was calibrated using the PTM state (see paragraph that follows) for 665 atoms that transformed from FCC to HCP or to an unidentified configuration that OVITO classified as Other. It was determined that atoms identified as FCC by PTM all had Q6 values greater than 0.49. A threshold for Q6 was therefore set to 0.49 to identify atoms that departed from an FCC configuration. All the atoms that were identified by PTM as having an HCP configuration had Q6 values in the range of 0.44–0.49. Atoms identified as Other had a wide range of Q6 values (from 0.3 to 0.55), and thus Q6 could not be directly correlated with the atoms classified by PTM as Other.

Visualization of the atomic positions was conducted using OVITO software (Stukowski, 2009). Polyhedral template matching (PTM

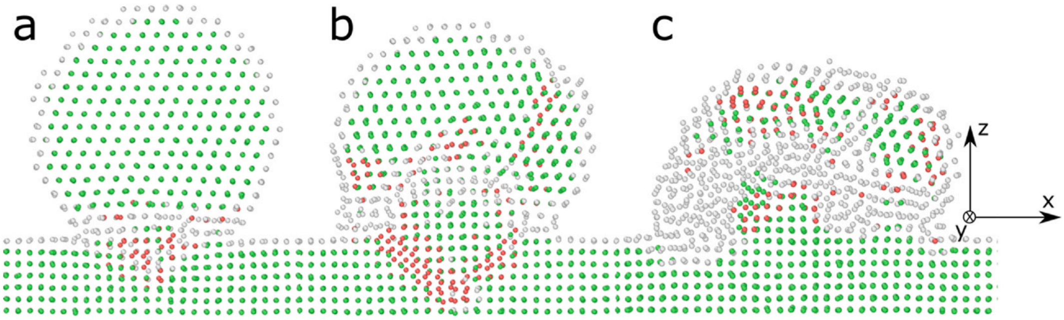

Fig. 2. Snapshots showing particle shape and atomic configuration for all three impact velocities that were simulated. The snapshots were taken at times near the peak particle deformation: a. 100 m/s at 7 ps, b. 300 m/s at 5 ps, and c. 600 m/s at 6 ps. Each image is a 1.1 nm thick slice through the center of the NP viewing a {110} surface. Atoms colored green have an FCC configuration, red have an HCP configuration, and gray are identified by PTM as Other. (For interpretation of the references to color in this figure legend, the reader is referred to the Web version of this article.)

command in OVITO) allows another method for assessing the local crystal structure for the atoms (Larsen et al., 2016). PTM compares the positions of atoms, their neighbors and next-nearest neighbors to positions in templates of reference atomic structures. A match is assigned to the lowest root mean square deviation (RMSD) below the set threshold. Unlike the Q6 parameter, PTM provides a discrete assessment of atomic configurations. We set the RMSD threshold within the normal range and eliminated crystal structures (false positives) that were not reasonable for Ag atoms (i.e., we retained only FCC, HCP, or unidentified structures and rejected BCC, which is observed in MD simulations only at extremely high pressures beyond the experienced in this study, and those structures that are not observed for Ag). In our PTM visualizations, a cutoff value of the RMSD threshold of 0.12 was used, which produced results that agreed with visual inspections of ordered and disordered regions of the simulations. The visualizations that are presented are color-coded with crystal structure information obtained from PTM, with green representing local regions of FCC stacking and red representing regions with a local HCP stacking, and gray being not identified and classified as Other (disordered).

3. Results

3.1. Maximum temperature rise

To determine if disordering transformations that were observed during impact resulted from melting or instead resulted from solid state amorphization, the maximum temperature experienced by atoms that were tracked was determined. The maximum temperature rise for an atom was computed from the relationship $T = (2/3)(KE/k_b)$, where k_b = the Boltzmann constant and KE = the atom's kinetic energy. The results can be classified by the impact velocities. For $v = 100$ m/s, negligible heating was observed for all the atoms that were tracked, and the peak temperatures for all cases remained below 400 K. For an impact velocity of 300 m/s, the maximum temperature experienced by the tracked atoms was between 500 and 700 K. For an impact velocity of 600 m/s, the maximum temperatures experienced by tracked atoms generally ranged between 600 and 800 K, with two atoms reaching 800–900 K. None of the peak temperatures approached the bulk melting temperature for Ag (1235 K measured from experiments and 1266 K for the EAM potential that was used). Furthermore, no cases reached the predicted reduced melting temperature for a 4.5 nm Ag particle (~960 K) (Luo et al., 2008). From this we can conclude that the observed disordering transformation results from solid-state amorphization and not from melting.

3.2. Minimum strain rate for amorphization

We previously have shown that for single-crystal bars uniformly loaded uniaxially, the critical strain rate required to induce amorphization is not a material property but instead depends on the orientation the crystal relative to the direction(s) of loading. Critical strain rates for Ag ranged from 5×10^{10} to 2×10^{11} s^{-1} for uniform uniaxial loading, depending on the loading direction and crystal orientation (Becker & Kovar, 2020). We have also shown that in biaxial loading, the critical strain rate also depends on strain state and a critical strain rate ranging from 1×10^{11} to 4×10^{11} s^{-1} was observed (Becker & Kovar, 2021). In this paper, we explore the minimum critical strain rate to initiate amorphization of non-uniformly loaded, individual atoms during particle impact. To do this, the von Mises shear strain was spatially averaged for the atoms of interest and their 12 nearest neighbors. The minimum strain rate to induce amorphization was determined for atoms that exhibited amorphization from the slope of the strain versus time plot. It was found that the minimum average strain rate to induce amorphization was 5×10^{10} s^{-1} for the particle impact simulations that were conducted. This shows that the minimum critical strain rate to induce amorphization during particle impact is similar to that required for uniform strain states.

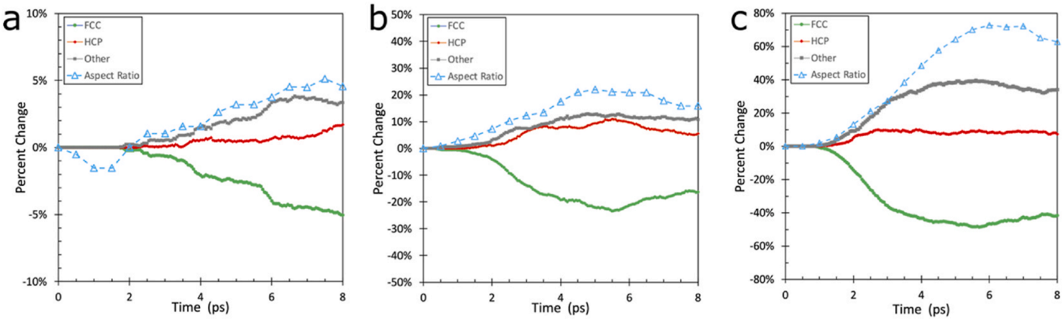

Fig. 3. Percent change in number of atoms present in the impacting particle identified by PTM as FCC, HCP, and Other, and NP aspect ratio change vs. time for impacts at velocity: a. 100 m/s, b. 300 m/s, and c. 600 m/s. The reference number of atoms used to calculate the percent changes are the 2792 atoms contained in the NP.

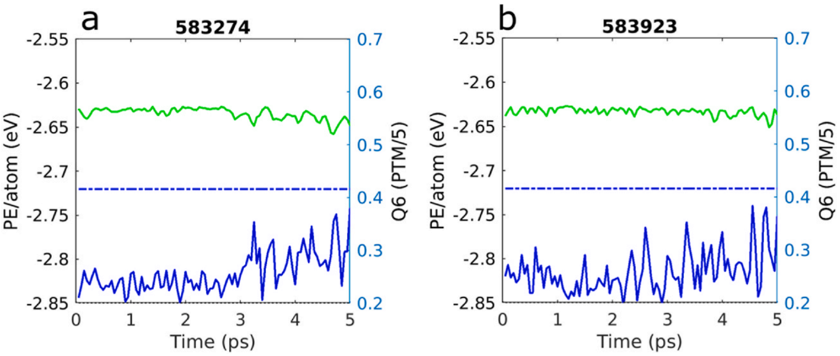

Fig. 4. PE/atom for two individual atoms for $v = 100$ m/s is plotted in dark blue versus time for: a. atom 583274 and b. atom 583923. See Fig. 1 and Table 1 for the locations of these atoms. The Q6 parameter is plotted in light green versus time. A dark blue, dash-dot horizontal line at a PE/atom of -2.72 eV is the proposed critical PE/atom to induce amorphization. The PTM configurations for both atoms remain in the FCC configuration (PTM $= 0.2$) throughout the simulations. (For interpretation of the references to color in this figure legend, the reader is referred to the Web version of this article.)

3.3. Atomic configurations and deformation during particle impact: representative examples

We next present an overview of the simulation results that show the effects of impact velocity on changes in atomic configurations and particle deformation. Snapshots of atom positions are shown in Fig. 2 after impact at the approximate time of maximum deformation and with PTM encoding used to identify the local atom configurations. Fig. 2a shows that for an impact velocity of 100 m/s, the particle remains nearly spherical, indicating that there is minimal overall deformation of the impacting particle. Examination of the atomic configurations shows that most of the atoms remain in the FCC configuration, but surface atoms are identified by PTM as Other because of the disruption of the nearest neighbor configurations caused by the surface. There is also an isolated region near the interface between the particle and substrate where a small number of atoms in both the particle and substrate are either identified as Other or as HCP.

Fig. 2b shows a snapshot near the time of maximum deformation for an impact velocity of 300 m/s. The atoms in the upper half of the particle remain FCC and are largely unaffected by the impact. However, the impacted particle exhibits a more flattened appearance resulting from greater deformation compared to the particle impacted at slower velocity shown in Fig. 2a. Stacking faults caused by partial dislocation motion are more prominent in both the particle and substrate, and the number of atoms within the particle that are identified as Other is also greater. Interestingly, atoms near the center of the impact interface are also FCC and epitaxial with the substrate. Observations of the atomic configurations at intermediate time steps (not shown) reveal that this epitaxial region is a result of devitrification after previously amorphizing.

Fig. 2c is a snapshot for an impact velocity of 600 m/s that shows even greater deformation of the particle as evidenced by the much larger aspect ratio (the ratio of the maximum width in the x direction to the maximum height in z above the substrate surface). At this particle impact velocity, a significant fraction of the atoms in the particle have changed configuration to Other, and these transformed atoms extend to near the top of the particle. These results show that the extent of deformation and amorphization that occurs in the impacting particle increases significantly for impact velocities of 600 m/s.

Fig. 3 shows plots that quantify the changes in the atomic configurations and aspect ratios for particles impacting at velocities from 100 to 600 m/s. The exact times of impact for each simulation velocity are 2.0 ps at 100 m/s, 0.3 ps for 300 m/s and 0.8 ps for 600 m/s.

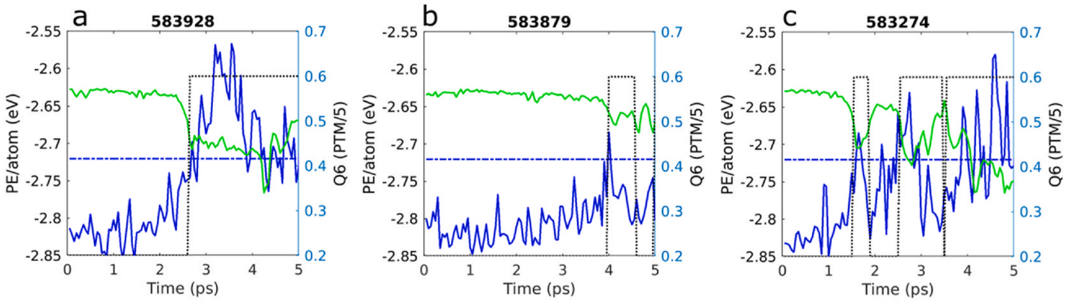

Fig. 5. PE/atom for representative individual atoms that amorphize is plotted in dark blue versus time. The Q6 parameter is plotted in light green versus time, and the discrete PTM state (FCC = 0.2, HCP = 0.4, and Other = 0.6) is plotted as a black, dotted line. A dark blue, dash-dot horizontal line at a PE/atom of −2.72 eV is the proposed critical PE/atom to produce amorphization. The NP velocities are 300 m/s in a, 100 m/s in b, and 600 m/s in c. See Fig. 1 and Table 1 for the locations of the atoms that are identified here by their atom id numbers at the top of each plot. (For interpretation of the references to color in this figure legend, the reader is referred to the Web version of this article.)

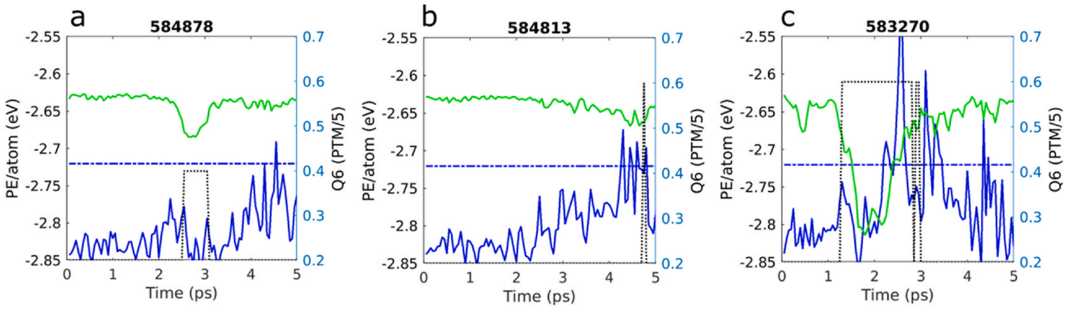

Fig. 6. PE/atom for individual atoms that show noteworthy behaviors is plotted in dark blue versus time. The Q6 parameter is plotted in light green versus time, and the discrete PTM state (FCC = 0.2, HCP = 0.4, and Other = 0.6) is plotted as a black, dotted line. A dark blue, dash-dot horizontal line at a PE/atom of −2.72 eV is the proposed critical PE/atom to produce amorphization. The NP velocities are 300 m/s in a and c and 100 m/s in b. See Fig. 1 and Table 1 for the locations of the atoms that are identified here by their atom id numbers at the top of each plot. (For interpretation of the references to color in this figure legend, the reader is referred to the Web version of this article.)

Each impact time is consistent among all of Figs. 2–6. Fig. 3a shows that for an impact velocity of 100 m/s there is a slight attractive elongation of the particle (decrease in aspect ratio) due to the attractive term of the EAM potential during the slow approach before true impact at 2 ps. This small distortion of the NP and of the substrate is visible in careful examination of the atom images, but it is smaller at higher impact velocities due to the shorter transit time available to overcome atomic inertia. After 2 ps, there is a small decrease in percentage of atoms identified by PTM as FCC and a corresponding increase of atoms identified as Other as well as a very small increase in the number of atoms identified as HCP. The total percentage change in atom configurations is less than 5%. Also shown in this plot is the change in aspect ratio, expressed as a percentage change from the equilibrated particle aspect ratio. Increases in the aspect ratio begin at the same time as changes occur in the atomic configurations. The cumulative increase in aspect ratio is limited to only about 5% at 7 ps.

Fig. 3b shows the changes in atomic configurations and aspect ratios for a particle impacting at a velocity of 300 m/s. Significant changes in atomic configuration are apparent beginning 1 ps after impact, which is also the time when the particle aspect ratio begins to increase. The percentage change in the number of atoms exhibiting an FCC configuration steadily decreases and plateaus after 5 ps at about a 25% reduction. The percent increase in HCP atoms is about 11% and the percent increase in Other atoms is about 13%. The aspect ratio increases as the atomic configurations are changing and reaches a maximum of a 22% increase around 5 ps.

Fig. 3c shows the changes in atomic configurations and aspect ratios for a particle impacting at a velocity of 600 m/s. At this higher velocity, significant changes in atomic configuration are again apparent 1 ps after impact. The percentage change in the number of atoms exhibiting an FCC configuration decreases to a much greater extent than was observed in Fig. 3a or 3b at lower impact velocities; it decreases by nearly 50%. Most of this decrease occurs due to an increase in Other atoms, with a relatively smaller percentage of atoms transforming to an HCP configuration. The aspect ratio also increases by over 70%, consistent with the significant flattening of the particle that is visually apparent for impact at this velocity. We have previously shown that deformation in Ag at higher strain rates occurs due to amorphization followed by viscous flow, and these results for an impact velocity of 600 m/s are consistent with our earlier visual observations (Chitrakar et al., 2017, 2019).

Collectively, Figs. 2 and 3 show that the overall deformation experienced by an impacting particle can be quantified by the changes in particle aspect ratio. These changes in particle shape occur at the same time as changes in atomic configuration, and the magnitude of the changes in both metrics increase with impact velocity. Moreover, the atomic-scale mechanisms responsible for the overall

Table 1
Atom identification numbers for the selected atoms (shown in Fig. 1). The identification numbers are arranged in the same geometrical pattern as they appear in Fig. 1.

Row #	Atom identification number			
9	584082	583996	584878	
8		583994		
7	583431	583928	584832	
6	583912	585490	584816	
5	583973	583923	583274	584813
4	583879	585480		
3	583270	583877	584705	

particle deformation can be assessed from the changes in local atomic configurations. For the current simulations, we see an increase in the number of atoms in an HCP configuration at moderate impact velocities ($v = 300$ m/s) compared to low impact velocities ($v = 100$ m/s). It has previously been shown that a local HCP configuration results from the passage of Shockley partial dislocations in FCC metals that leads to the formation of stacking faults (Chitrakar et al., 2017). Thus, the presence of these local HCP regions suggests that some of the observed deformation results from dislocation plasticity. As the impact velocity is increased to higher velocities ($v = 600$ m/s), the fraction of the atoms that transform to Other increases, which confirms that amorphization/viscous flow becomes the primary mechanism for plasticity during particle impact at this higher velocity.

3.4. Predicting local amorphization during particle impact using the PE/atom criterion

A series of simulations were conducted to test the hypothesis that a critical PE/atom of at least −2.72 eV is required to initiate the onset of amorphization in local regions of an Ag particle that may exhibit a range of strain rates, strain states and potential energies. To do this we first consider representative individual atoms within particles impacting at a range of velocities from 100 to 600 m/s because, as shown in Figs. 2 and 3, these velocities produce a range of deformation behaviors depending on the location within the particle. This allows us to critically test the hypothesis by examining the PE/atom and the corresponding atomic configurations for atoms at various locations within the particle during impact. Figs. 4–6 show plots of the PE/atom versus time for different atoms (See Fig. 1 and Table 1 for the locations of the atoms that are identified here by their atom identification numbers at the top of each graph.). Also shown in each plot are two time-dependent metrics (the Q6 parameter and the discrete PTM state) that allow the atomic configuration for that atom to be assessed. PTM was initially encoded as integers 1–3 for FCC, HCP, and Other. For display in the figures on the same right axis as Q6, PTM is divided by 5 yielding values 0.2, 0.4 and 0.6 for FCC, HCP, and Other respectively (noted as PTM/5).

When interpreting the time-dependent plots that follow, it is worth noting the time intervals required for an acoustic wave, a dislocation, and the gross strain or atomic crushing to travel up through the particle as it impacts. The longitudinal sound velocity in silver is 3.65 nm/ps, and the particle impact velocities are 0.1, 0.3 and 0.6 nm/ps. It takes 0.6 ps for an acoustic wave to reach the uppermost atoms selected for study and somewhat longer for a dislocation to propagate this distance at an observed velocity of about 2 nm/ps. The strain wave or crushing of the atoms can reach the center of the particle in 3 ps (for impact at 300 m/s) and to the top of the particle in 5 ps if the deformation mechanisms allow it to propagate that far. The following analysis of threshold behavior for these cases is based on the *first* time that an atom passes threshold, even though some cases transition back and forth between disorder and FCC ordering several times during the deformation process, which lasts up to 6–7 ps. Thus, the tracked atoms are observed for the first 5 ps to include their first possible disordering event.

Fig. 4 shows two representative cases for atoms in particles impacted at $v = 100$ m/s. For both cases the PE/atom (shown in dark blue) prior to impact is about −2.82 eV, with a standard deviation of ±0.02 eV due to thermal fluctuations. Fig. 4a (atom 583274) shows that about 3.2 ps after impact there is an increase in the PE/atom when the strain wave from the impact reaches the location of this atom, and the magnitude of the fluctuations in PE/atom then increases slightly. The PE/atom remains well below the critical PE/atom of −2.72 eV, and the PTM state indicates that the atomic configuration remains in the FCC configuration throughout the simulation. Fig. 4b (atom 583923) shows the behavior of another atom that exhibits some larger fluctuations in the PE/atom when the strain wave arrives at the atom. Although the peak PE/atom exceeds −2.76 eV, the PTM state remains FCC, and the Q6 parameter remains above 0.49 indicating that no transformation in atomic configuration has occurred. This figure shows that when the PE/atom remains below the critical PE/atom of −2.72 eV, amorphization does not occur.

Fig. 5 shows the behavior of representative atoms in particles impacted at three different velocities that are all observed to amorphize upon impact. In Fig. 5a (atom 583928), the PE/atom for this atom (impact at 300 m/s) begins to increase sharply about 2 ps after impact and it exceeds −2.72 eV about 2.7 ps after impact. The PE/atom continues to increase reaching a peak of about −2.57 eV before decaying back to about −2.72 eV about 5 ps after impact. At nearly the same time that the PE/atom first exceeds −2.72 eV, the Q6 parameter (shown in light green) drops sharply from about 0.57 to about 0.43 and the PTM state (black dashed line) increases from 0.2 to 0.6 (Other). Both changes are consistent with a persistent transformation in atomic configuration from FCC to amorphized. This case illustrates a typical response observed when the PE/atom rises above −2.72 eV for a sustained period.

Fig. 5b and c shows the responses of two additional atoms that amorphize. The atom shown in Fig. 5b (atom 583879) exhibits an increase in PE/atom near 4 ps after impact at 100 m/s. Like the response of the atom shown in Fig. 5a, as the PE/atom exceeds −2.72 eV, both the Q6 parameter and the PTM state indicate a transformation from FCC to amorphized. However, in this case, the PE/atom

Table 2
Data for disorder/no-disorder statistics. The time that each criterion passed the disorder threshold is recorded in the table. Blank rows did not disorder for all three criteria. One case was identified as a transition to HCP configuration (noted as HCP), and for one case (noted as-), Q6 failed to reach threshold.

100 m/s	identification	FIRST TIME TO PASS THRESHOLD (ps)		
atom no.	number	PE/atom	Q6	PTM Other
1	583877	3.525	3.925	3.775
2	583879	3.975	4.575	3.975
3	585480	1.775	4.925	4.725
4	583274			
5	583923			
6	583912			
7	584816			
8	585490			
9	583928			
10	583270	2.825	2.675	2.675
11	583431			
12	583973			
13	583994			
14	584082			
15	583996			
16	584705	4.525	3.525	3.275
17	584813	4.275	-–	4.725
18	584832			
19	584878			
300 m/s		PE/atom	Q6	PTM
1	583877	2.625	1.525	1.475
2	583879	2.075	1.975	1.925
3	585480	2.125	2.075	2.025
4	583274	1.975	2.425	2.275
5	583923	2.225	2.275	2.225
6	583912	2.475	2.475	2.525
7	584816	1.725	2.325	2.125
8	585490	2.625	2.425	2.375
9	583928	2.675	2.625	2.625
10	583270	2.175	0.425	1.275
11	583431	3.725	3.775	3.725
12	583973	3.025	2.625	2.725
13	583994	3.825	3.275	3.675
14	584082	4.625	4.575	4.425
15	583996	4.325	4.325	4.275
16	584705	1.625	1.475	1.625
17	584813	1.575	1.825	2.675
18	584832	2.575	2.375	2.875
19	584878	4.525	2.525	HCP
600 m/s		PE/atom	Q6	PTM
1	583877	1.275	1.425	1.225
2	583879	1.225	1.425	1.425
3	585480	1.425	2.025	1.625
4	583274	1.575	1.575	1.525
5	583923	1.375	1.525	1.525
6	583912	3.275	2.375	2.425
7	584816	1.625	1.675	1.625
8	585490	1.625	1.725	1.625
9	583928	2.125	2.675	2.675
10	583270	1.725	1.225	1.275
11	583431	2.025	2.225	2.025
12	583973	1.775	2.125	2.125
13	583994	2.325	2.725	2.725
14	584082	2.225	2.325	2.325
15	583996	2.425	2.825	2.825
16	584705	0.725	1.525	1.525
17	584813	1.325	1.375	1.825
18	584832	1.675	1.825	1.775
19	584878	2.425	3.025	1.975

only slightly exceeds −2.72 eV, and then it immediately falls below this threshold upon transformation of the atomic structure. The PE/atom drops and the atomic structure to reverts to FCC. Fig. 5c (atom 583274) shows an atom for an impact at 600 m/s that exhibits repetitive transformations into and out of an amorphous configuration when the PE/atom exceeds −2.72 eV. The first transition to an amorphous configuration occurs at 1.5 ps, lasts for a very short time, and the atomic configuration then immediately reverts to FCC

Table 3
Frequency table for the 57 cases from Table 2 for a [111] NP incident on a [001] surface at 100, 300, and 600 m/s. An atom is classified as disordered if both Q6 and PTM state indicate disordering.

	Atom observed to disorder	Atom not disordered
PE/atom above threshold	42	2
PE/atom blow threshold	0	13

Statistical significance level, $p < 4.2 \times 10^{-11}$ (Fisher Exact Test).

when the PE/atom falls below −2.72 eV. The atom transforms a second time to the amorphous configuration when the PE/atom again rises above −2.72 eV, but as the PE/atom again falls below the threshold, briefly reverts to the FCC configuration, before amorphizing for a third time with a short time delay after the PE/atom threshold is exceeded. This transformation and reversion response is typical of what was observed when the PE/atom does not stay above the critical PE/atom of −2.72 eV for a sustained period of time or does not rise significantly above the critical PE/atom. These simulations confirm that increases of the PE/atom for individual atoms experiencing nonuniform stress states above the proposed threshold of −2.72 eV result in transformation to the amorphous configuration. The simulations also show that after the initial transformation, the atomic configuration may or may not be stable depending on how far above and for how long the PE/atom remains above the critical PE/atom. For this reason, we will consider only the initial transformation in the subsequent discussion.

Fig. 6 illustrates behaviors of specific atoms that, while not typical, illustrate other noteworthy complexities that may arise. Fig. 6a (atom 584878) shows an example (impact at 300 m/s) where a slight increase is observed in the PE/atom when the strain wave arrives at this atom's location about 2.2 ps after impact, but the PE/atom remains well below the threshold for amorphization. At this time, the PTM state indicates a transformation to HCP, and the Q6 parameter falls to a value of between 0.44 and 0.49, consistent with, but not definitively indicating, that this atom has transformed to an HCP configuration. As discussed earlier, a transformation to HCP results from a stacking fault when a partial dislocation passes through this region of the crystal.

Fig. 6b (atom 584813) and 6c (atom 584270) show examples where the time when the PE/atom first exceeds the critical PE/atom is not coincident with the transformation in atomic configuration indicated by PTM. In Fig. 6b, the amorphization transformation occurs about 0.5 ps after the PE/atom exceeds the critical PE/atom. Although Q6 decreases at the same time as the PE/atom, it does not dip below the threshold value. In addition, the atom in Fig. 6b is in row 5 of the particle which also includes the two atoms shown in Fig. 4 that do not disorder. In Fig. 6c, the transformation to Other and the time when Q6 goes below threshold occur about 1 ps before the PE/atom exceeds the critical PE/atom. These discrepancies in timing can occur because, for this analysis, we have only considered the PE/atom for individual atoms. As discussed further in section 3.6 and in the discussion section, fluctuations in PE/atom can also affect the timing of the amorphization transformation.

3.5. Statistics for correct classification of amorphized atoms using the PE/atom criterion

Although Figs. 4–6 illustrate representative behaviors that are consistent with the proposed PE/atom criterion, a critical assessment of the PE/atom criterion for predicting amorphization requires a rigorous statistical analysis of the data. To do this, the 19 atoms that are shown in Fig. 1 were tracked for impact velocities of 100, 300, and 600 m/s (i.e., a total of 57 cases were considered). A summary of the results is presented here; the raw data are presented in Table 2. The frequency table for this data is shown in Table 3, and the significance is

$p < 4.2 \times 10^{-11}$ using the Fisher exact test (for data with <5 in some cells).

There were 42 cases where the PE/atom exceeded the critical PE/atom and both the Q6 parameter and the PTM parameter identified a transformation to the amorphized state. All of these 42 cases were correctly classified by the PE/atom criterion. There were an additional 13 cases where the PE/atom remained below the critical PE/atom, and both the Q6 parameter and the PTM parameter indicated that no transformation to the amorphized state occurred. Thus, the PE/atom criterion correctly classified the amorphization transformation in 55 out of the 57 cases that were considered (96.5% accuracy).

We now consider more carefully the two cases that were not correctly predicted by the critical PE/atom criterion. Atom 584813 was in a particle impacted at 100 m/s where the PE/atom exceeded the critical PE/atom and the PTM parameter briefly changed the atom's classification to Other. Although the Q6 parameter dropped, it did not drop below 0.49 to indicate a transformation away from an FCC configuration. In the second case, atom 584878 was in a particle impacted at 300 m/s, where the PE/atom exceeded the critical PE/atom and the Q6 parameter dropped to below 0.49 to indicate a transformation away from an FCC configuration. However, the PTM parameter did not change to Other as predicted, but instead changed to HCP, which suggests the presence of a dislocation. These two cases are truly borderline cases in which there is disagreement between the two measures used to determine the atomic configuration. This illustrates that even small local fluctuations in atom position or temperature can influence the atomic configuration and thus highlights the importance of a considering a statistically significant number of atoms in assessing the ability of the critical PE/atom criterion in predicting amorphization. A discussion of the physical causes of fluctuations is presented in the discussion section.

To provide more statistical robustness to our results, additional simulations beyond those presented in Table 2 were conducted for a different particle crystal orientation relative to the impact axis at velocities that generated borderline cases, 100 and 300 m/s. These additional simulations tracked 38 atoms for each impact velocity for a 4.5 nm particle incident along its [101] axis on a (001) substate surface. The region for selection and the random atom selection process was the same as described for the [111] incidence case except that more atoms were chosen within the region. For the 76 cases, 73 atoms remained in the measurement volume so that parameters

Table 4

Disorder/no-disorder statistics for simulation of a 4.5 nm Ag [101] oriented particle on [001] oriented substrate. The time that each criterion passed its respective threshold is recorded in the table. Blank rows did not disorder for all three criteria. For cases that are borderline, non-threshold measures are shown as -. Failed cases, where the atom left the measurement volume, are excluded from the statistics and are shown as an X.

100 m/s	atom id	FIRST TIME TO PASS THRESHOLD (ps)		
		PE/atom	Q6	PTM
1	583245	3.825	4.125	4.125
2	583239	5.075	5.275	5.525
3	583307			
4	583296			
5	583393			
6	583831	4.175	4.625	4.325
7	585376	2.025	2.475	2.425
8	583835	3.325	4.325	3.475
9	583872			
10	583863			
11	583900			
12	583972			
13	583902			
14	583917			
15	583996			
16	584638	2.375	2.525	2.475
17	584735	4.625	5.475	5.175
18	584785	–	5.725	5.825
19	584805			
20	583852			
21	584817			
22	583295			
23	584852			
24	584861			
25	585381			
26	585378	3.325	–	–
27	X	X	X	X
28	585460			
29	585356	4.675	4.825	4.925
30	585474	4.825	–	–
31	585494			
32	585408			
33	585481			
34	58549			
35	585567			
36	585546			
37	585562			
38	585569			
300 m/s		PE/atom	Q6	PTM
1	583245	1.825	1.775	1.825
2	583239	1.825	1.525	1.825
3	583307	1.175	1.475	1.525
4	583296	4.175	4.325	4.175
5	X	X	X	X
6	583831	1.275	1.625	1.625
7	585376	0.575	0.775	0.775
8	583835	1.025	1.725	1.675
9	583872	2.075	2.575	2.575
10	583863	2.425	3.375	3.375
11	583900	2.825	3.825	3.825
12	583972	3.075	4.675	4.675
13	583902	2.975	4.675	4.725
14	583917	2.425	3.825	3.775
15	583996	2.275	–	–
16	584638	0.325	0.725	0.675
17	584735	2.025	2.475	2.325
18	584785	2.325	2.025	1.925
19	584805	2.675	3.275	3.575
20	583852	2.925	3.075	3.125
21	584817	1.725	2.925	2.575
22	583295	4.375	4.475	4.375
23	584852	6.025	4.825	5.675
24	584861	4.375	4.375	4.375
25	585381	2.175	1.575	1.925

(*continued on next page*)

Table 4 (*continued*)

100 m/s	atom id	FIRST TIME TO PASS THRESHOLD (ps)		
		PE/atom	Q6	PTM
26	585378	0.775	1.375	1.575
27	585458	2.375	2.725	2.975
28	585460	2.425	3.025	2.975
29	585356	1.325	1.725	1.725
30	585474	1.025	2.625	2.475
31	585494	2.725	2.825	3.925
32	585408	1.925	2.075	1.925
33	585506	1.575	1.975	2.025
34	X	X	X	X
35	585498	4.525	4.175	3.925
36	585567	4.975	4.675	4.975
37	585546	3.325	–	–
38	585562	4.625	4.675	5.725

Table 5
Frequency table for the 73 cases from Table 4 for a [101] NP incident on a [001] surface at 100 and 300 m/s. An atom is classified as disordered if both Q6 and PTM state indicate disordering.

	Atom observed to disorder	Atom not disordered
PE/atom above threshold	42	4
PE/atom blow threshold	1	26

Statistical significance level, $p < 1.8 \times 10^{-7}$ (Fisher Exact Test).

could be tracked. All three parameters agreed regarding amorphization (or no amorphization) 93.2% of the time. The raw data for this analysis are shown in Table 4. The frequency table for this data is shown in Table 5, and the significance is $p < 1.8 \times 10^{-7}$ using the Fisher exact test. For 4 of the 5 borderline cases, a brief peak in PE/atom exceeded threshold while both PTM and Q6 did not indicate amorphization. In the remaining case, both Q6 and PTM indicated amorphization within 0.2 ps of the end of the simulation, but PE/atom had not yet passed threshold. In total, aggregating the classification statistics for all 130 cases from Tables 3 and 5 results in rejection of the null hypothesis (random classification) at $p < 2.2 \times 10^{-8}$ using the Fisher exact test (for data with >5 in some cells). Thus, the PE/atom criterion is found to be a highly significant classifier of atom amorphization.

3.6. *Time differentials between PE/atom and atom disorder criteria reaching threshold*

Several criteria have been proposed to predict the onset of amorphization based on changes in physical properties or other parameters (Born, 1939; Egami & Waseda, 1984; Kulp et al., 1993; Lindemann, 1910; Okamoto et al., 1988; Rosato & Massobrio, 1993; Seidel et al., 1988; Wang et al., 1993a, 1993b). We previously showed that for uniformly loaded single crystals, one advantage of the PE/atom criterion is that it *predicts* amorphization because changes in PE/atom occur *before* atomic configuration measures indicate amorphization has occurred. Other measures of amorphization such as an abrupt temperature rise or strain-based criteria are lagging indicators of amorphization (Becker & Kovar, 2020, 2021). To assess whether PE/atom is also a leading indicator for amorphization for the non-uniform strain state and strain rates that arise during NP impacts, we measured the first threshold onset times for the three parameters (PE/atom, Q6, and PTM) for the simulations conducted in this study (shown in Tables 3 and 5). It is important to assess whether the large standard deviation in times between when amorphization is predicted and when it initiates is due to a few outliers or whether this is a consistent trend for all atoms. To accomplish this, a statistical method is employed for assessing whether the critical PE/atom led or lagged the onset of amorphization. All 84 cases that displayed amorphization are considered for this analysis, and PE/atom was leading for 54 cases and lagging for 30 cases. When testing this binomial distribution, the integrated probability of the null hypothesis (that leading and lagging cases are randomly distributed) is rejected at the $p < 0.01$ level ($p = 0.006$). So, we conclude that PE/atom is a significant leading indicator of atom disordering.

4. Discussion and conclusions

The results of the MD simulations conducted for this study confirmed the hypothesis that a critical PE/atom criterion is a leading indicator for high strain rate disordering of individual atoms under the highly non-uniform conditions experienced during particle impact. The critical PE/atom for disordering of individual atoms of Ag was found to be the same (−2.72 eV) for non-uniform loading as was previously determined for uniform loading (Becker & Kovar, 2020, 2021). For comparison, the energy difference between the equilibrium PE/atom at 300 K and the critical PE/atom is 0.10 eV/atom, the latent heat of melting for Ag is 0.112 eV/atom, the energy of formation for a vacancy is 1.081 eV/atom, and the energy of formation for an octahedral interstitial is 3.026 eV/atom. The temperatures experienced during particle impact were found to be well below the melting temperature, confirming that disordering was due to amorphization rather than melting.

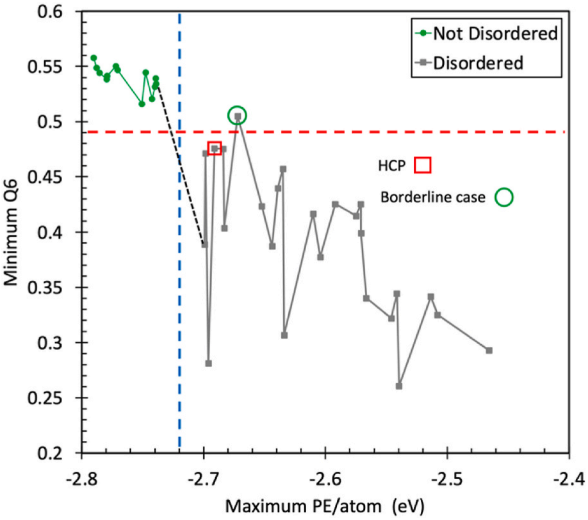

Fig. 7. Minimum value of Q6 vs. maximum value of PE/atom plotted for each tracked atom for NP impacts at 100 and 300 m/s. The threshold for transformation indicated by Q6 is the red, dashed horizontal line, and the threshold for PE/atom is the blue, dashed vertical line. The black, dotted line is a guide that connects the rightmost not-disordered point with the leftmost disordered point. The two atoms showing borderline behavior are marked. (For interpretation of the references to color in this figure legend, the reader is referred to the Web version of this article.)

An assessment was carried out to determine whether the critical PE/atom criterion is a leading indicator of amorphization. This analysis showed that for a statistically significant fraction of the cases, the critical PE/atom was reached before transformation to the amorphous state occurred. However, there were considerable variations observed in the time differentials between predictions for disordering and the observed change in atomic configurations. Notably, the two measures used for assessing atomic configuration (Q6 parameter and PTM state) also often exhibited significant time differentials.

Another indicator by which to evaluate the discrimination quality of the PE/atom criterion can be seen by distributing the cases according to their *maximum* PE/atom and their *minimum* Q6 parameter over the entire 5 ps time span. This discrimination function is illustrated in Fig. 7 by plotting the minimum Q6 parameter vs. the maximum PE/atom for the cases of [111] particle impacts at 100 and 300 m/s. The prediction of PTM classification (Disordered or Not Disordered) is noted on the plot by line color and point shape. The two borderline cases discussed in section 3.5 are also indicated. For impact at 600 m/s, all the selected atoms disordered, and they would be plotted in the lower-right quadrant of Fig. 7 (but they are not shown for clarity). The power of PE/atom as a discriminator for amorphization is clearly shown by the segregation of the data points into the 2nd and 4th quadrants. Also well illustrated is the possibility of borderline cases arising due to fluctuations (standard deviation ≈ ±0.03 eV) in PE/atom near the threshold value. This borderline region is remarkably narrow, and it is clear that these fluctuations can span the gap between disordered and not disordered cases and result in a few borderline cases. Although the maximum PE/atom and the minimum Q6 do not necessarily occur at the same time, and they do not necessarily occur at the same time as the threshold crossings, Fig. 7 illustrates the strength of the PE/atom upward excursion and the strength of the Q6 downward excursion correlate well with the amorphization predictions of the three parameters.

Our simulation results show that the PE/atom fluctuates with time and that these fluctuations affect: 1) classification of amorphous atoms in borderline cases, 2) the timing of the amorphization transformation relative to when it is predicted, and 3) the stability of the amorphous configuration relative to the crystalline state. We now consider whether these fluctuations are an artifact of the simulation methodology or whether there is a physical cause for the fluctuations. To do this we analyzed the PE/atom for a representative number of atoms of interest and their nearest neighbors during particle impact and during uniform loading. We found that thermal fluctuations produced typical fluctuations in PE/atom of ±0.02 eV at room temperature, with larger fluctuations when temperature or loading increased. These thermal fluctuations are largely uncorrelated with nearest neighbor atoms. However, other physical phenomena can result in correlated motions between atoms and their nearest neighbors. One example is the passage of partial dislocation in a neighboring atom, which we found temporarily decreases the PE/atom of the atom of interest. Other examples of temporally and spatially correlated atom motions are from the passage of a shock wave or a phonon. These correlated atomic motions may result in the observed discrepancies between the prediction of amorphization and the observed atomic disordering. This effect was strongest for borderline cases where the excursion above the critical PE/atom was short-lived or where neighboring atoms had a relatively high PE/atom compared to the atom of interest due to a local fluctuation. Although these fluctuations produce a small fraction of outliers, the critical PE/atom was nevertheless found to correctly predict atomic-scale amorphization under highly non-uniform conditions in the vast majority of the cases that were studied.

Availability of data

The data that support the findings of this study are available from the corresponding author upon reasonable request.

Declaration of competing interest

The authors declare that they have no known competing financial interests or personal relationships that could have appeared to influence the work reported in this paper.

Acknowledgements

This work was supported by the National Science Foundation under Grant Nos. CMMI 1435949 and CMMI 2102818. The authors acknowledge the Texas Advanced Computing Center (TACC) at The University of Texas at Austin for providing HPC resources that have contributed to the research results reported in this paper. URL: http://tacc.utexas.edu.

References

Akedo, J., Lebedev, M., Nakano, S., & Ogiso, H. (2003). Aerosol deposition for nanocomposite material synthesis: A novel method for ceramics processing without firing. *Ceramic Engineering and Science Proceedings, 24*(3), 9–14.

Becker, M. F., & Kovar, D. (2020). A quantitative criterion for predicting solid-state disordering during high strain rate deformation. *Journal of Physics: Condensed Matter, 33*(6), Article 065405.

Becker, M. F., & Kovar, D. (2021). A quantitative criterion for predicting solid-state disordering during biaxial, high strain rate deformation. *Modelling and Simulation in Materials Science and Engineering, 30*(1), Article 015006. https://doi.org/10.1088/1361-651x/ac3cca

Born, M. (1939). Thermodynamics of crystals and melting. *The Journal of Chemical Physics, 7*(8), 591–603. https://doi.org/10.1063/1.1750497

Chitrakar, T. V., Keto, J. W., Becker, M. F., & Kovar, D. (2017). Particle deposition and deformation from high speed impaction of Ag nanoparticles. *Acta Materialia, 135*, 252–262. doi: 0.1016/j.actamat.2017.05.062.

Chitrakar, T. V., Noiseau, G. J. J., Keto, J. W., Becker, M. F., & Kovar, D. (2019). An experimental and computational study of high-speediImpact of Ag nanoparticles. *Journal of Applied Physics, 125*, Article 195104. https://doi.org/10.1063/1.5063345

Egami, T., & Waseda, Y. (1984). Atomic size effect on the formability of metallic glasses. *Journal of Non-crystalline Solids, 64*(1), 113–134. https://doi.org/10.1016/0022-3093(84)90210-2

Hanft, D., Exner, J., Schubert, M., Stöcker, T., Fuierer, P., & Moos, R. (2015). An overview of the aerosol deposition method: Process fundamentals and new trends in materials applications. *Journal of Ceramic Science and Technology, 6*(3), 147–182. https://doi.org/10.4416/JCST2015-00018

Huang, C., Nichols, W. T., O'Brien, D. T., Becker, M. F., Keto, J. W., & Kovar, D. (2007). Supersonic jet deposition of silver nanoparticle aerosols: Correlations of impact conditions and film morphologies. *Journal of Applied Physics, 101*, Article 064902.

Ikeda, H., Qi, Y., Çagin, T., Samwer, K., Johnson, W. L., & Goddard, W. A. (1999). Strain rate induced amorphization in metallic nanowires. *Physical Review Letters, 82*(14), 2900–2903. https://doi.org/10.1103/PhysRevLett.82.2900

Kashu, S., Fuchita, E., Manabe, T., & Hayashi, C. (1984). Deposition of ultra fine particles using a gas jet. *Japnese Journal of Applied Physics, 23*(12A), L910–L912.

Kulp, D. T., Egami, T., Luzzi, D. E., & Vitek, V. (1993). A molecular dynamics study of atomic level stress distributions in defective intermetallics. *Journal of Alloys and Compounds, 194*(2), 417–427. https://doi.org/10.1016/0925-8388(93)90027-K

Larsen, P. M., Schmidt, S., & Schiøtz, J. (2016). Robust structural identification via polyhedral template matching. *Modelling and Simulation in Materials Science and Engineering, 24*(5), Article 055007. https://doi.org/10.1088/0965-0393/24/5/055007

Lindemann, F. A. (1910). The calculation of molecular vibration frequencies. *Zeitschrift für Physik, 11*, 609–612.

Luo, W., Hu, W., & Xiao, S. (2008). Size effect on the thermodynamic properties of silver nanoparticles. *Journal of Physical Chemistry C, 112*, 2359–2369.

McCallister, J. J. H., Gammage, M. D., Keto, J. W., Becker, M. F., & Kovar, D. (2021). Influence of agglomerate morphology on micro cold spray of Ag nanopowders. *Journal of Aerosol Science, 151*, Article 105648. https://doi.org/10.1016/j.jaerosci.2020.105648

Mickel, W., Kapfer, S. C., Schröder-Turk, G. E., & Mecke, K. (2013). Shortcomings of the bond orientational order parameters for the analysis of disordered particulate matter. *The Journal of Chemical Physics, 138*(4), Article 044501. https://doi.org/10.1063/1.4774084

Ogawa, H. (2005). Molecular dynamics simulation on the single particle impacts in the aerosol deposition proces. *Materials Transactions, 46*(6), 1235–1239.

Ogawa, H. (2006). Atomistic simulation of the aerosol deposition method with zirconia nanoparticles. *Materials Transactions, 47*(8), 1945–1948. https://doi.org/10.2320/matertrans.47.1945

Okamoto, P. R., Rehn, L. E., Pearson, J., Bhadra, R., & Grimsditch, M. (1988). Brillouin scattering and transmission electron microscopy studies of radiation-induced elastic softening, disordering and amorphization of intermetallic compounds. *Journal of the Less Common Metals, 140*, 231–244. https://doi.org/10.1016/0022-5088(88)90384-0

Park, H., Kwon, J., Lee, I., & Lee, C. (2015). Shock-induced plasticity and fragmentation phenomena during alumina deposition in the vacuum kinetic spraying process. *Scripta Materialia, 100*, 44–47. https://doi.org/10.1016/j.scriptamat.2014.12.008

Plimpton, S. (1995). Fast parallel algorithms for short-range molecular dynamics. *Journal of Computational Physics, 117*, 1–19.

Rosato, V., & Massobrio, C. (1993). The role of chemical disorder and volume expansion in crystal-to-amorphous transitions: Simulation results for $NiZr_2$ and Cu_3Au. *Journal of Alloys and Compounds, 194*(2), 439–445. https://doi.org/10.1016/0925-8388(93)90029-M

Seidel, A., Massing, S., Strehlau, B., & Linker, G. (1988). Amorphous phase formation in Mn-implanted Al films and single crystals. *Physical Review B, 38*(4), 2273–2282. https://doi.org/10.1103/PhysRevB.38.2273

Shinoda, W., Shiga, M., & Mikami, M. (2004). Rapid estimation of elastic constants by molecular dynamics simulation under constant stress. *Physical Review B, 69*(13), Article 134103. https://doi.org/10.1103/PhysRevB.69.134103

Steinhardt, P. J., Nelson, D. R., & Ronchetti, M. (1983). Bond-orientational order in liquids and glasses. *Physical Review B, 28*(2), 784–805. https://doi.org/10.1103/PhysRevB.28.784

Stukowski, A. (2009). Visualization and analysis of atomistic simulation data with OVITO–the Open Visualization Tool. *Modelling and Simulation in Materials Science and Engineering, 18*(1), Article 015012. https://doi.org/10.1088/0965-0393/18/1/015012

Wang, F., Gao, Y., Zhu, T., & Zhao, J. (2011). Shock-induced breaking of the nanowire with the dependence of crystallographic orientation and strain rate. *Nanoscale Research Letters, 6*(1), 291. https://doi.org/10.1186/1556-276X-6-291

Wang, J., Yip, S., Phillpot, S., & Wolf, D. (1993a). Intrinsic response of crystals to pure dilatation. *Journal of Alloys and Compounds, 194*(2), 407–415. https://doi.org/10.1016/0925-8388(93)90026-J

Wang, J., Yip, S., Phillpot, S. R., & Wolf, D. (1993b). Crystal instabilities at finite strain. *Physical Review Letters, 71*(25), 4182–4185. https://doi.org/10.1103/PhysRevLett.71.4182

Williams, P. L., Mishin, Y., & Hamilton, J. C. (2006). An embedded-atom potential for the Cu–Ag system. *Modelling and Simulation in Materials Science and Engineering, 14*(5), 817–833.